Materials Advances

ROYAL SOCIETY OF CHEMISTRY

PAPER

View Article Online
View Journal | View Issue

Open Access Article. Published on 11 March 2024. Downloaded on 7/23/2025 9:33:46 PM.
This article is licensed under a Creative Commons Attribution-NonCommercial 3.0 Unported Licence.

Check for updates

Cite this: *Mater. Adv.*, 2024, 5, 3424

Insights into the interfaces of VO_2(M) and VO_2(B) polymorphs with different substrates

Elaheh Mohebbi,[a] Eleonora Pavoni,[a] Luca Pierantoni,[b] Pierluigi Stipa,[a] Emiliano Laudadio *[a] and Davide Mencarelli[b]

Received 16th January 2024,
Accepted 26th February 2024

DOI: 10.1039/d4ma00048j

rsc.li/materials-advances

The phenomena arising at the interface between oxide materials and substrates can fundamentally and practically change the physical and chemical properties of the materials themselves. In this study, we employed density functional theory (DFT) calculations to elucidate the stability and optical properties of VO_2(M) and VO_2(B) interactions with substrates of sapphire(*c*-cut), sapphire(*r*-cut), $SrTiO_3$(001), $SrTiO_3$(111), $SrNbO_3$(001), $SrNbO_3$(111), $LaAlO_3$(*c*-cut), and $LaAlO_3$(*r*-cut). The surface calculations showed that the fully relaxed $SrTiO_3$(111) and $SrNbO_3$(001) possess the highest energies of 31.8 eV nm^{-2} and 21.15 eV nm^{-2} relative to other slabs, before optimizing with VO_2(M) and VO_2(B) polymorphs, respectively. The calculated adsorption energy indicated that the interface of VO_2(M) and VO_2(B) structures showed more stability on $SrTiO_3$(001) and $SrTiO_3$(111), with adsorption energy values of 2.83 eV and 0.91 eV, respectively. Furthermore, the optical absorption properties of the highest and lowest stable interfaces have been evaluated. The outcomes predicted that VO_2(M)@$SrTiO_3$(001) and VO_2(B)@$SrTiO_3$(111) have their optical adsorption in the visible light range, while VO_2(M)@sapphire(*c*-cut) and VO_2(B)@sapphire(*c*-cut) showed the main adsorption peak in the infrared region.

Introduction

Epitaxial synthesis of heterostructure oxides has shown considerable promise in creating new functionalities and chemical–physical properties by controlling some parameters, such as lattice, spin, charge, and orbital order.[1] Heterostructures of oxide materials allow for tuning the electronic, magnetic, and optical properties, as well as giving rise to emergent behaviours that are distinct from the bulk properties of either material. Since there are no substrates available with similar structures (lattice parameters and crystal symmetry), the ability to grow the thin films of binary oxides like TiO_2[2] and VO_2[3,4] on lattice- and symmetry-mismatched substrates is of crucial importance for discovering their unprecedented potential.

It is well known that vanadium oxides (VO_2) represent an abundant and diverse family of compounds with multipurpose applications. VO_2 exists in multiform polymorphic stable and metastable forms, including rutile VO_2(R),[5] monoclinic VO_2(M),[6] and triclinic VO_2(T) phases,[7] that are similar in structure. But there are other four VO_2 phases designated as tetragonal VO_2(A),[8] monoclinic VO_2(B),[9] paramontroseite VO_2,[10] and VO_2 with a new body centered-cubic (bcc) structure.[11] Among them, VO_2(M) possesses a fully reversible metal–insulator phase transition to the most stable VO_2(R), associated with the benefits of huge temperature-induced resistivity changes as well as the selective optical switches, which have received great interest in industrial and scientific areas for construction of intelligent devices such as temperature sensors,[12] GHz operating frequency,[13] thermochromics,[14] and energy efficient smart windows.[14] On the other hand, the VO_2(B) phase has also been explored as a promising cathode material in Li-ion batteries, not only on the basis of its appropriate electrode potential, but also its particular tunnelled structure.[15] However, metastable VO_2(B) is a relatively less-studied polymorph in comparison to the other oxides of vanadium.

Recently, our group has carried out a comprehensive DFT-study on the characterization of the geometry, stability, Raman spectra, and the electronic, magnetic, and optical properties of VO_2(M)[16] and VO_2(B)[17,18] nanostructures. The study on the electronic band gap of VO_2(M)[16] based on the Heyd–Scuseria–Ernzerhof (HSE)[19] functional showed excellent agreement with photoemission experiments (band gap ∼ 0.6–0.7 eV)[20] by a band gap of 0.6 eV. In addition to the improved prediction of the peak position in the absorption spectra with the same functional, this method also described reasonably well the static dielectric constant of 7.54 of VO_2(M), showing an excellent match with the experimental values. In an experimental work by Lourembam *et al.*,[21] they have investigated the photo-induced insulator-to-metal transition in VO_2(B) using the

[a] *Department of Matter, Environmental Sciences, and Urban Planning, Marche Polytechnic University, 60131 Ancona, Italy. E-mail: e.laudadio@staff.univpm.it*
[b] *Information Engineering Department, Marche Polytechnic University, 60131 Ancona, Italy*

© 2024 The Author(s). Published by the Royal Society of Chemistry

Open Access Article. Published on 11 March 2024. Downloaded on 7/23/2025 9:33:46 PM.
This article is licensed under a Creative Commons Attribution-NonCommercial 3.0 Unported Licence.

temperature-dependent optical pump–probe technique. This study reported the metallic phase (300 K) and the insulating phase (100 K) of this structure, respectively; however, the insulating phase can be indicated by two electronic relaxation times and the metallic phase showed only one characteristic time. Our recently study[17] based on the use of PBEsol[22] demonstrated for the first time the experimental metallic-like phase of VO_2(B).

So far, using pulsed laser epitaxy (PLE), high quality VO_2(M) and VO_2(B) thin films were successfully stabilized on perovskite substrates like $SrTiO_3$. Chen *et al.*[23] reported that the textured VO_2(B) thin film with a layered structure was grown on $SrTiO_3$(001) by pulsed laser deposition. In addition, a small amount of the VO_2(M) phase can co-grow in the VO_2(B) phase. This study indicates an alternative approach to enhance the performance of insulating VO_2(B) based batteries by increasing

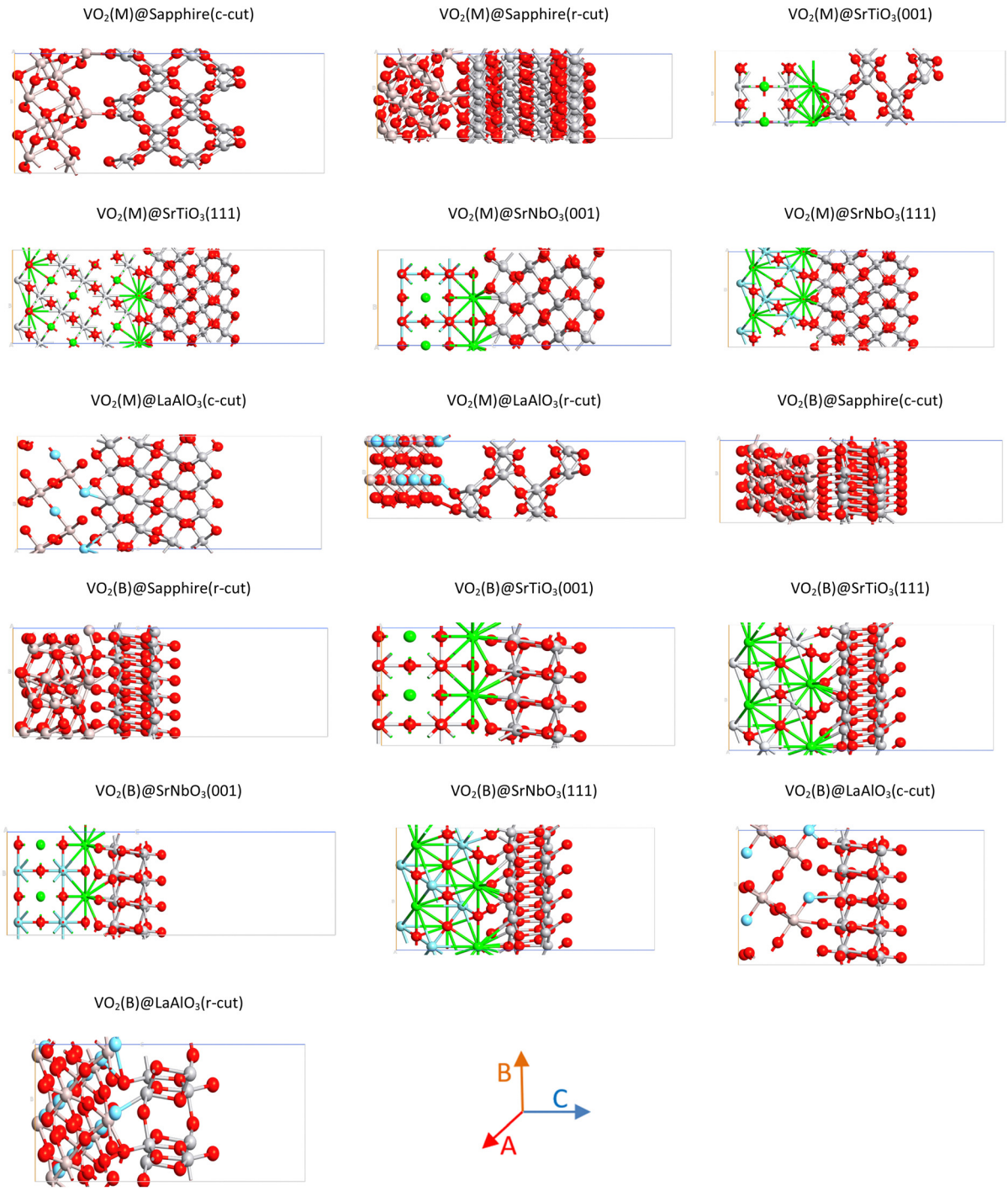

Fig. 1 Schematic representations of VO_2(M) and VO_2(B) material interfaces with different substrates. The color code in the ball and stick models: V grey, O red, Al pink, Sr green, Nb cyan, Ti silver, and La light blue.

Open Access Article. Published on 11 March 2024. Downloaded on 7/23/2025 9:33:46 PM.
This article is licensed under a Creative Commons Attribution-NonCommercial 3.0 Unported Licence.

the electrical conductivity. Srivastava *et al.*[24] demonstrated the novel heterostructures of high-quality single-phase films of VO_2 (A and B) on the $SrTiO_3$ substrate by controlling the vanadium arrival rate (laser frequency) and oxidation of the V atoms. In addition, the *c*-plane Al_2O_3 (sapphire) substrate has been used to consider the first phase transition stability of VO_2 thin films grown *via* both *ex situ* heating and *in situ* heating by transmission electron microscopy (TEM). Electrical resistance measurements were conducted on the VO_2 thin films to characterize the semiconductor to metallic transition (SMT) properties during multiple thermal cycles. *In situ* TEM heating experiments were conducted to investigate the film microstructure evolutions during phase transition cycles.[25]

In this work, using DFT calculations, for the first time, we reported the stability and optical properties of different interfaces of VO_2(M) and VO_2(B) on sapphire(*c*-cut), sapphire(*r*-cut), $SrTiO_3$(001), $SrTiO_3$(111), Nb substituted with Ti in $SrNbO_3$(001) and $SrNbO_3$(111), $LaAlO_3$(*c*-cut), and $LaAlO_3$(*r*-cut) surfaces and used these results to understand how two dissimilar materials can form heterostructures with different characterizations. Computational advances in the atomic-scale simulations of oxide heterostructures are able to provide a fertile new ground for creating novel states at their interfaces and varied symmetry constraints can be used to design structures exhibiting phenomena that are not found in the bulk constituents and then that can be exploitable in practical device applications of VO_2.

Results and discussion

Initially, the slab of various configurations was modelled; then, different interfaces, as seen in Fig. 1, were constructed by the interactions between the slabs and the VO_2(M) and VO_2(B) perpendicular to the surface along the *z* direction. All the information related to the crystal structure and lattice parameters for substrates of Al_2O_3, $SrTiO_3$ and $LaAlO_3$ as well as VO_2(M and B) polymorphs are reported in Table 1. Moreover, the details related to the lattice dimensions for different interfaces are reported in Table 2. It is evident from our computational results that after the structural relaxation of all supercells, the vertical distances between VO_2 (M and B) and different facets of $SrTiO_3$ and $SrNbO_3$ are lower (an average interface distance of 2.37 Å) than those for Al_2O_3 and $LaAlO_3$ substrates. The outcomes indicate that the adsorption is primarily dominated by the vdW interactions on the substrates of sapphire facets and even in La-containing slabs, with vertical distances around 3.63 Å. By considering the chemical properties of different elements like electron configuration, atomic radius and electronegativity, as shown in Table 3, since the vanadium (V) atom has a small atomic radius of 134 pm and an electronegativity of 1.63, the charges can transfer more easily with strontium (Sr), having an electronegativity of 0.91 and a bigger radius sphere of 255 pm, compared to aluminium (Al) with a similar electronegativity of 1.61 and an atomic radius of 1.43. When we used the $SrNbO_3$ and $LaAlO_3$ substrates, still we get the direct connections of Sr–V and Al–V in the interfaces, and the chemical properties of Nb and La atoms could not significantly affect the chemical properties of vanadium atoms. The comparison between titanium (Ti) (niobium (Nb)) in $SrTiO_3$ ($SrNbO_3$) substrates indicates that the charges can transfer more easily with titanium (Ti), having an electronegativity of 1.54 and a smaller radius sphere of 187 pm, compared to Nb with a similar electronegativity of 1.60 but a bigger atomic radius of 207 pm. The same condition exists for the La atom in $LaAlO_3$ which has a bigger atomic radius (250 pm) than Al (143 pm). However, as we see later, the presence of these elements can influence less the stability of heterostructures.

After simulating all interface systems, we removed VO_2(M) and VO_2(B) polymorphs from the supercells and we evaluated the surface energy of different relaxed surfaces. The theoretical formalism for evaluating the surface energy can be expressed from the following formula:[26]

Table 1 Crystal structure and lattice parameters for substrates and VO_2 (M and B) polymorphs

Bulk systems	Crystal structure (space group)	Lattice constant			
		a (Å)	*b* (Å)	*c* (Å)	*β* (°)
Al_2O_3	Trigonal ($R\bar{3}C$)	4.81	4.81	13.12	120
$SrTiO_3$	Cubic ($Pm\bar{3}m$)	3.95	3.95	3.95	90
$LaAlO_3$	Trigonal ($R\bar{3}C$)	5.41	5.41	13.19	120
VO_2(M)	Monoclinic ($P2_1/c$)	5.38	4.52	5.74	122.6
VO_2(B)	Monoclinic ($C2/m$)	12.03	3.69	6.42	106

Table 2 Lattice dimensions for different interfaces of VO_2(M and B) polymorphs

Interface	*a* (Å)	*b* (Å)	*c* (Å)	*β* (°)
VO_2(M)@sapphire(*c*-cut)	9.61	10.35	21.61	62.35
VO_2(M)@sapphire(*r*-cut)	18.34	7.06	21.07	118.11
VO_2(M)@$SrTiO_3$(001)	11.15	7.89	23.29	45
VO_2(M)@$SrTiO_3$(111)	11.15	11.15	22.27	60
VO_2(M)@$SrNbO_3$(001)	11.15	7.89	20.27	45
VO_2(M)@$SrNbO_3$(111)	11.15	11.15	24.07	60
VO_2(M)@$LaAlO_3$(*c*-cut)	10.82	10.78	22.62	120.112
VO_2(M)@$LaAlO_3$(*r*-cut)	23.55	5.39	22.31	90.26
VO_2(B)@sapphire(*c*-cut)	17.35	11.06	20.01	15.25
VO_2(B)@sapphire(*r*-cut)	16.94	7.71	22.30	95.36
VO_2(B)@$SrTiO_3$(001)	11.83	7.89	18.39	90
VO_2(B)@$SrTiO_3$(111)	12.51	11.15	19.43	120
VO_2(B)@$SrNbO_3$(001)	11.83	7.89	28.92	90
VO_2(B)@$SrNbO_3$(111)	11.15	11.15	19.07	120
VO_2(B)@$LaAlO_3$(*c*-cut)	10.82	10.78	17.42	59.88
VO_2(B)@$LaAlO_3$(*r*-cut)	17.85	10.78	16.87	41.24

Table 3 Chemical properties of different elements in materials

Element	Electron configuration	Atomic radius (pm)	Electronegativity
Sr(Ti, Nb)O_3			
Sr	[Kr] $5s^2$	255	0.95
Ti	[Ar] $3d^24s^2$	187	1.54
Nb	[Kr] $4d^45s^1$	207	1.60
Al(Al, La)O_3			
Al	[Ne] $3s^23p^1$	143	1.61
La	[Xe] $5d^16s^2$	250	1.10
VO_2			
V	[Ar] $3d^34s^2$	134	1.63

 © 2024 The Author(s). Published by the Royal Society of Chemistry

Open Access Article. Published on 11 March 2024. Downloaded on 7/23/2025 9:33:46 PM.
This article is licensed under a Creative Commons Attribution-NonCommercial 3.0 Unported Licence.

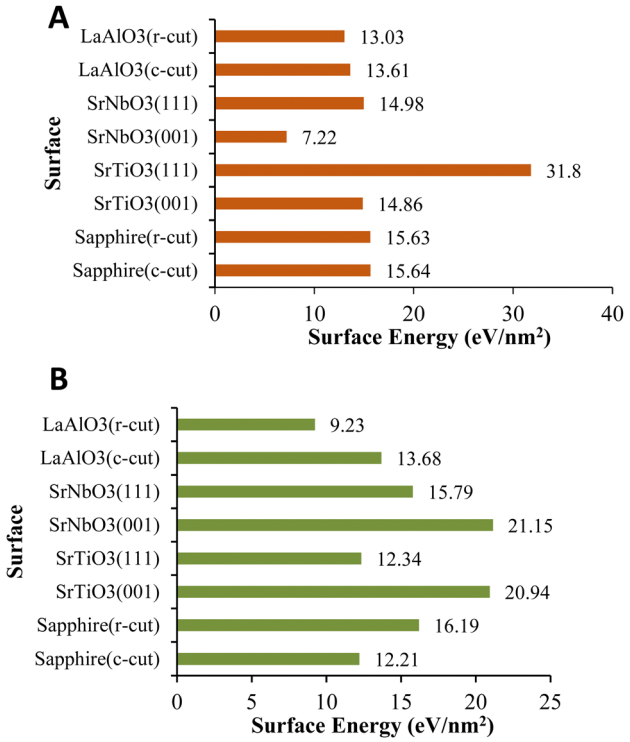

Fig. 2 Surface energy for relaxed different slabs of sapphire(*c*-cut), sapphire(*r*-cut), $SrTiO_3$(001), $SrTiO_3$(111), $SrNbO_3$(001), $SrNbO_3$(111), $LaAlO_3$(*c*-cut), and $LaAlO_3$(*r*-cut) before optimizing with VO_2(M) (A) and VO_2(B) (B) polymorphs.

$$E_s = E(n) + nE_{Bulk}/2A \quad (1)$$

where A is the area of the primitive surface unit cell, $E(n)$ refers to the energy of a slab with n formula units, and E_{Bulk} is the energy of a formula unit of the bulk material. The results of the present DFT calculations of the surface energy for different slabs are summarized in Fig. 2, where all the calculations are related to the fully relaxed slabs.

As can be seen, in the case of VO_2(M), the surface energy of fully relaxed $SrTiO_3$(111) is considerably larger than all the slabs with 31.8 eV nm^{-2}; however, the surface energy of sapphire(*c*-plane) has a similar magnitude to those of sapphire(*r*-plane), $SrNbO_3$(111), and $SrTiO_3$(001) by values of 15.65 eV nm^{-2}, 15.63 eV nm^{-2}, 14.98 eV nm^{-2}, and 14.86 eV nm^{-2}, respectively. The magnitude of the relaxed surface energies for $SrNbO_3$(001) is lower than that for all the slabs with 7.22 eV nm^{-2} and some middle surface energy values can be observed for $LaAlO_3$(*c*-cut) (13.61 eV nm^{-2}) and $LaAlO_3$(*r*-cut) (13.03 eV nm^{-2}). Inspections of Fig. 2 show that the surface energy of different interfaces with the VO_2(B) polymorph assumed different values, in the order of $SrNbO_3$(001) > $SrTiO_3$(001) > sapphire(*r*-cut) > $SrNbO_3$(111) > $LaAlO_3$(*c*-cut) > $SrTiO_3$(111) > sapphire(*c*-cut) > $LaAlO_3$(*c*-cut) with the surface energies of 21.15 > 20.94 > 16.19 > 15.79 > 13.68 > 12.34 > 12.21> 9.23 eV nm^{-2}, respectively. Woo *et al.*[27] also concluded the surface energy of 28–34 eV nm^{-2} of $SrTiO_3$(111) as the most stable facet of $SrTiO_3$. In fact, there is also reasonably good qualitative agreement with the theoretical results of Stirner *et al.*[28] who obtain the relative surface energies of various sapphire surfaces with the ratios of 11–30 eV nm^{-2} for the *c*-plane and 14–19 eV nm^{-2} for the *r*-plane. It is also interesting to note from Fig. 2 that, amongst these different surface facets, *r*- and *c*-plane $LaAlO_3$ have shown the middle surface energy in good consistency with that shown in ref. 29 in which the surface energy of 5–29 eV nm^{-2} is reported for the *c*-plane face of this substrate.

To find the most stable geometric configurations, we investigated the adsorption energy of VO_2(M) and VO_2(B) on different surfaces (Fig. 3). We calculated the adsorption of different interfaces using the following eqn (2)[30,31]

$$E_{ads} = E_{VO_2(x)} + E_{substrate} - E_{VO_2(x)+substrate} \quad (2)$$

where $E_{substrate}$ refers to the total energies of isolated VO_2 (M, or B) and substrates and $E_{VO_2(x)+substrate}$ is the total energy of the interface system. Our data indicate that for VO_2(M) adsorption, sapphire(*c*-cut) and sapphire(*r*-cut) exhibit similar binding energies of 31.76 eV and 30.52 eV, respectively, owing to its weak physical interaction with no chemical bond formation directly corroborating to its larger vertical distance to VO_2 polymorphs and the values are significantly lower than those of $SrTiO_3$(001) (2.83 eV), $SrTiO_3$(111) (6.69 eV), $SrNbO_3$(001) (6.41 eV), and $SrNbO_3$(111) (10.46 eV), $LaAlO_3$(*c*-cut) (14.1 eV) and $LaAlO_3$(*r*-cut) (11.92 eV). The adsorption energies of VO_2(B) on the surfaces became stronger than those of VO_2(M). According to our DFT calculations, the calculated binding energies are 21.12, 1.11, 4.14, 0.91, 8.02, 6.39, 19.10 and 5.49 for sapphire(*c*-cut), sapphire(*r*-cut), $SrTiO_3$(001), $SrTiO_3$(111), $SrNbO_3$(001), $SrNbO_3$(111), $LaAlO_3$(*c*-cut), and $LaAlO_3$(*r*-cut) surfaces, respectively. We observe that the most stable interfaces for VO_2(M) and VO_2(B) structures are

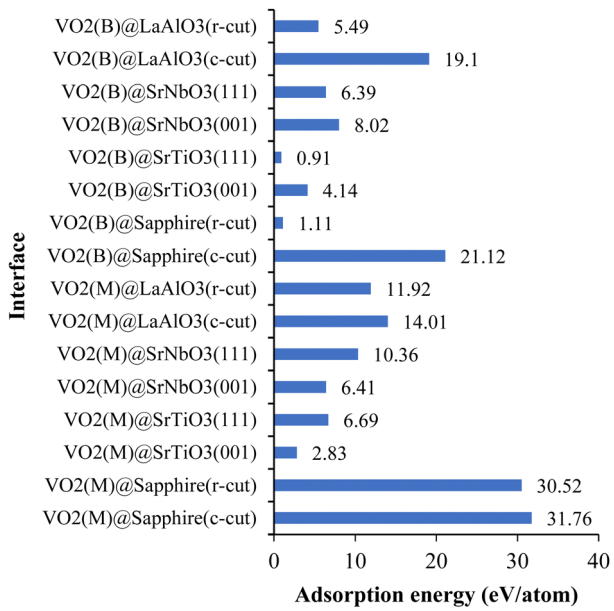

Fig. 3 Adsorption energy for different interfaces of VO_2(M and B) polymorphs on sapphire(*c*-cut), sapphire(*r*-cut), $SrTiO_3$(001), $SrTiO_3$(111), $SrNbO_3$(001), $SrNbO_3$(111), $LaAlO_3$(*c*-cut), and $LaAlO_3$(*r*-cut) substrates.

Open Access Article. Published on 11 March 2024. Downloaded on 7/23/2025 9:33:46 PM.
This article is licensed under a Creative Commons Attribution-NonCommercial 3.0 Unported Licence.

$SrTiO_3$(001) and $SrTiO_3$(111), while the less stable interfaces are related to sapphire(*c*-cut) for both polymorphs.

Optical properties

The absorption coefficients for VO_2(M) and VO_2(B) polymorphs on the VO_2(M)@sapphire(*c*-cut), VO_2(M)@$SrTiO_3$(001), VO_2(B)@sapphire(*c*-cut), and VO_2(B)@$SrTiO_3$(111) interfaces are plotted in Fig. 4, as the most (VO_2(M)@$SrTiO_3$(001) and VO_2(B)@$SrTiO_3$(111)) and less (VO_2(M)@sapphire(*c*-cut) and VO_2(B)@sapphire(*c*-cut)) stable interfaces, as we discussed before. Here, we reported the acquired results in the visible (from 380 to 780 nm) and infrared (from 780 to 2500 nm) ranges as a function of wavelength. Based on this figure and the range of photon energy, the maximum absorption coefficients are 28×10^4 cm^{-1} (at 500 nm) and 21×10^4 cm^{-1} (at 620 nm) for VO_2(M)@$SrTiO_3$(001) and VO_2(B)@$SrTiO_3$(111) along the *xx* in-plane direction in the central energy zone of visible light (green–yellow) and low energy part of the visible light (red), respectively. The corresponding values predicted for VO_2(M)@sapphire(*c*-cut) and VO_2(B)@sapphire(*c*-cut) are 24×10^4 cm^{-1} (at 1500 nm) and 19×10^4 cm^{-1} (at 1000 nm), along the in-plane direction, respectively, with the first main peaks of the absorption coefficient in the light infrared region of the electromagnetic spectrum.

We next discuss the dielectric constant of the four interfaces, as we assessed their optical adsorption. The real and imaginary parts of dielectric constant of VO_2(M)@sapphire (*c*-cut)(A), VO_2(M)@$SrTiO_3$(001)(B), VO_2(B)@sapphire(*c*-cut)(C), and VO_2(B)@$SrTiO_3$(111) (D) interfaces are presented in Fig. 5, as a function of energy (eV). The imaginary part of all interfaces began with a high intensity of VO_2(M)@sapphire(*c*-cut) (A), while the intensity of peaks dropped with that of VO_2(B)@$SrTiO_3$(111) (D). In addition, the optical edge, which is called the optical band gap, can be calculated for these systems by drawing a vertical line from the wall of the first peak to the horizontal *x*-axis and here the outcomes indicate that the optical band gap is zero in all cases. According to this study, a static real dielectric constant has its maximum values at 107, 76 and 36 along the *xx*-, *yy*- and *zz*-directions for VO_2(M)@sapphire(*c*-cut) (A), while the corresponding values have reduced to 61, 43, and 11 for VO_2(M)@$SrTiO_3$(001) (B) along the same directions, respectively. In comparison, VO_2(B) interfaces showed a lower static dielectric constant than VO_2(M) ones by 33, 22 and 12 for VO_2(B)@sapphire(*c*-cut) (C) and the lowest

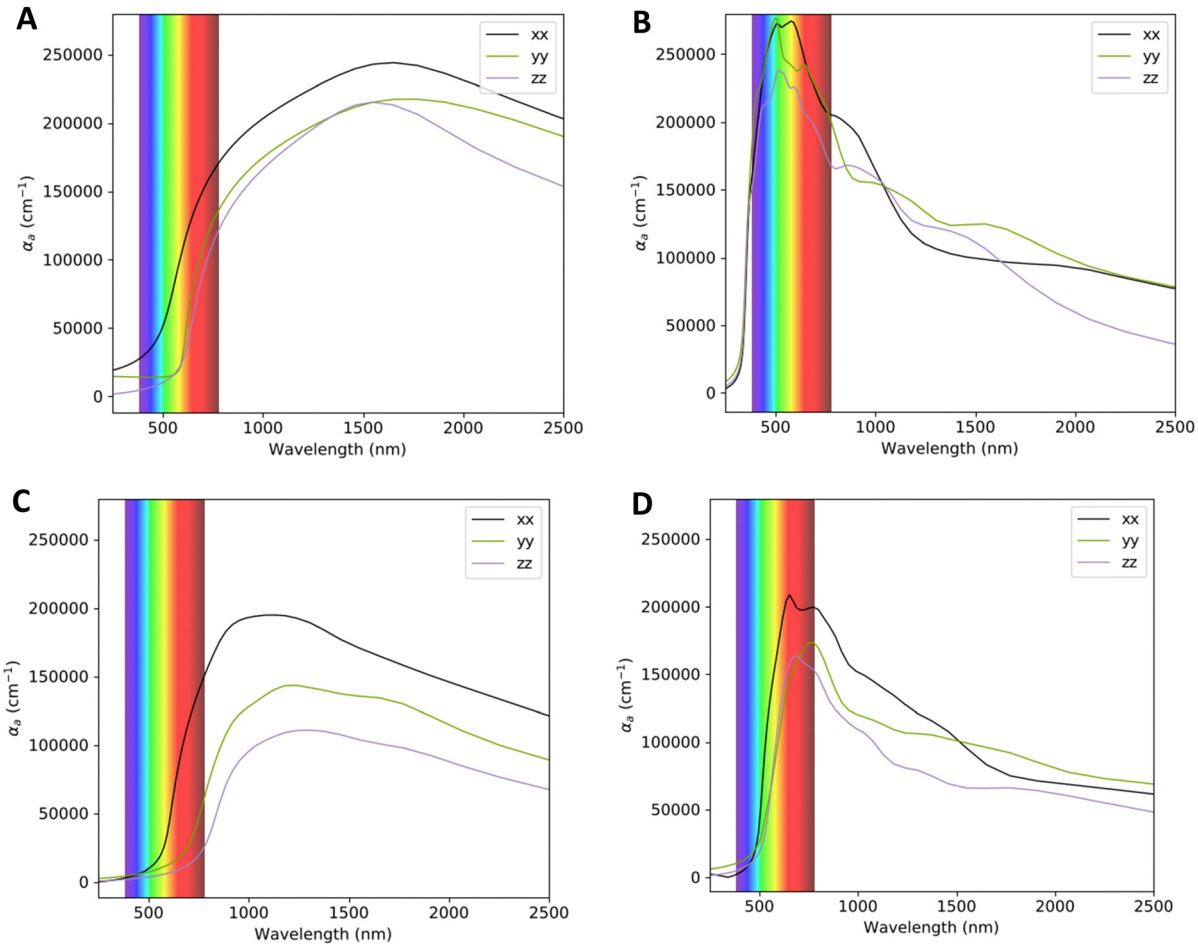

Fig. 4 Optical adsorption of VO_2(M)@sapphire(*c*-cut) (A), VO_2(M)@$SrTiO_3$(001) (B), VO_2(B)@sapphire(*c*-cut) (C), and VO_2(B)@$SrTiO_3$(111) (D) interfaces, as a function of the wavelength (nm) scale.

 © 2024 The Author(s). Published by the Royal Society of Chemistry

Open Access Article. Published on 11 March 2024. Downloaded on 7/23/2025 9:33:46 PM.
This article is licensed under a Creative Commons Attribution-NonCommercial 3.0 Unported Licence.

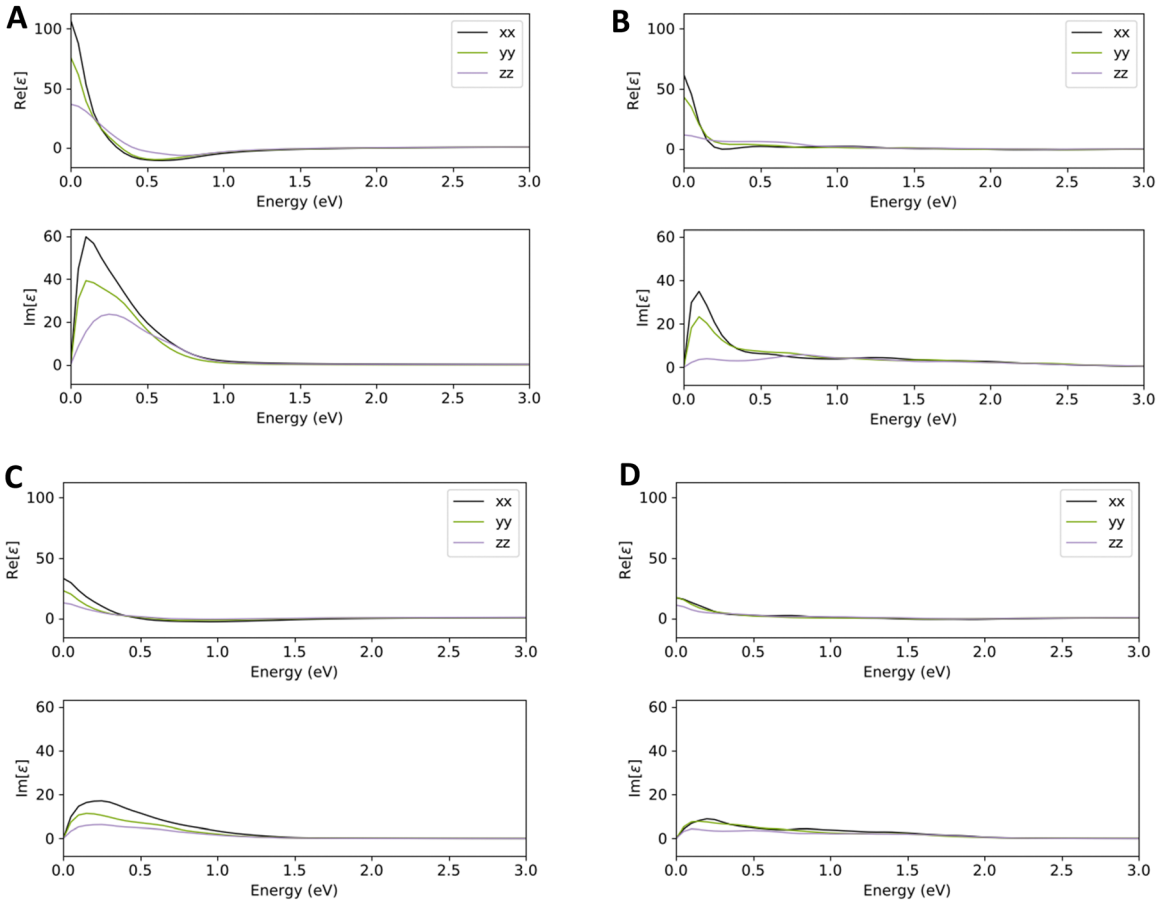

Fig. 5 Real and imaginary parts of dielectric constants of VO_2 (M)@sapphire(*c*-cut) (A), VO_2(M)@$SrTiO_3$(001) (B), VO_2 (B)@sapphire(*c*-cut) (C), and VO_2 (B)@$SrTiO_3$(111) (D) interfaces, at energy (eV) scale.

values for VO_2(B)@$SrTiO_3$(111) (D) with 17, 16 and 10 along the in-plane and out-of-plane directions, respectively. These theoretical advances in the optical adsorption and high dielectric constant further highlight the desirable performances of these proposed VO_2-based interfaces, suitable for photoelectronic applications such as solar energy conversion[32,33] and infrared light photodetectors[34,35] with high optical absorption in the visible and infrared regions, respectively.

According to the outcomes reported in the section "Results and discussion", by optimization of all four systems, the vertical distances between VO_2(M)/$SrTiO_3$ and VO_2(B)/$SrTiO_3$ layers showed lower values with respect to VO_2(M)/sapphire and VO_2(B)/sapphire interfaces. These equilibrium distances between the layers can efficiently influence the electronic band diagram of the interfaces such as the density of the charges of each element in the valence and conduction band edges. Moreover, the calculated adsorption energy for each heterostructure is in the same trend with the geometrical parameter results which reveal more interaction between VO_2(M)/VO_2(B) with the $SrTiO_3$ surface. It is worth to notice that all mentioned structural parameters and interface energies are induced by the large symmetry mismatch between the adsorbates and surfaces. On the other hand, while we observed the zero optical band gap for all four interfaces, the optical adsorption and dielectric constant of each material as well as substrate can affect the optical features of the total interface. As reported by previous studies, the imaginary and real part of the dielectric constant of $SrTiO_3$ shows the optical band gap in the visible range and a lower static dielectric constant[36] than sapphire with the infrared-active modes.[37,38] More interestingly, the formation of an interfacial layer composed of VO_2(B) on $SrTiO_3$ and sapphire by the larger symmetry mismatch (with respect to VO_2(M) interfaces) showed a lower dielectric constant (as seen in Fig. 5) to facilitate the symmetry transition between the two distinct component structures.

Methods

We carried out the atomistic calculations using the Quantum Atomistic ToolKit (QATK)[39] package. The DFT approach was implemented in the Kohn–Sham (KS) formulation,[40] within the framework of the linear combination of atomic orbitals (LCAO) basis set approach, combined with the pseudopotential (PPs) method and the Perdew–Burke–Ernzerhof (PBE) scheme of the generalized gradient approximation (GGA).[41] PseudoDojo[42] was used for the LCAO calculation to describe the interaction between ion cores and valence electrons. Valence orbitals were

Open Access Article. Published on 11 March 2024. Downloaded on 7/23/2025 9:33:46 PM.
This article is licensed under a Creative Commons Attribution-NonCommercial 3.0 Unported Licence.

considered with a kinetic energy cut-off of 90 Ry and a 3 × 3 × 1 Monkhorst–Pack *k*-point mesh was used. We used a vacuum spacing of 16–20 Å perpendicular to the basal planes to avoid image–image interactions across the periodic boundary. The geometries were optimized using a conjugate gradient algorithm where the atoms were allowed to relax until the residual force and energies were smaller than 0.025 eV $Å^{-1}$ and 1×10^{-4} eV, respectively. The Brillouin zone was integrated with Blöchl corrections using a broadening width of 0.005 eV.[43,44] The van der Waals corrections were included by Grimme's DFT-D3 method,[45,46] in order to include the dispersion corrections.

Optical calculations were evaluated based on the random phase approximation (RPA).[47] The optical properties of the interfaces in this study are discussed by the two components of the dielectric function $\varepsilon_1(\omega)$ and $\varepsilon_2(\omega)$ related to different polarizations in the electric field. The imaginary part $\varepsilon_2(\omega)$ of the dielectric coefficient can be obtained from the direct interband transitions through Fermi's golden rule as in eqn (3)[48–50]

$$\varepsilon_2(\omega) = \frac{4\pi^2}{\Omega\omega^2} \sum_{i\in HOMO, j\in LUMO} \sum_k W_k \left|\rho_{ij}\right|^2 \delta\left(\varepsilon_{kj} - \varepsilon_{ki} - h\omega\right) \quad (3)$$

where the HOMO, LUMO, ω, Ω, W_k, and ρ_{ij} denote the valence band, conduction band, photon frequency, volume of the lattice, weight of the *k*-point, and elements of the dipole transition matrix, respectively.

Moreover, the real part ($\varepsilon_1(\omega)$) of the dielectric constant can be obtained with the following eqn (4)

$$\varepsilon_1(\omega) = 1 + \frac{1}{\pi} P \int_0^\infty d\bar{\omega} \frac{\bar{\omega}\varepsilon_2(\bar{\omega})}{\bar{\omega}^2 - \omega^2} \quad (4)$$

We discussed the absorption coefficient ($\alpha_\alpha(\omega)$) which is ascribed by eqn (5):

$$\alpha_\alpha(\omega) = \frac{\omega \mathrm{Im}[\varepsilon_\alpha(\omega)]}{c n_\alpha(\omega)} \quad (5)$$

where c denotes the speed of light, and $n_\alpha(\omega)$ refers to the refractive index.

Conclusions

In this work, we used first-principles calculations to predict the adsorption of VO_2(M) and VO_2(B) structures on different substrates consisting of sapphire(*c*-cut), sapphire(*r*-cut), $SrTiO_3$(001), $SrTiO_3$(111), $SrNbO_3$(001), $SrNbO_3$(111), $LaAlO_3$(*c*-cut), and $LaAlO_3$(*r*-cut). Using cell optimization and total energy calculations, we compare the relative surface energy, adsorption energy, optical adsorption and dielectric constants of the interfaces. The surface energy calculations show that there is a considerable difference in relaxation of the slabs comparing the VO_2(M) and VO_2(B) polymorphs. A comparison between surfaces revealed that the surface energies of fully relaxed $SrTiO_3$(111) in VO_2(M) and $SrNbO_3$(001) in VO_2(B) have considerably larger surface energy than other slabs with 31.8 eV nm^{-2} and 21.15 eV nm^{-2}, respectively. The adsorption energy calculations revealed that the interface of the VO_2(M) polymorph is more favorable on $SrTiO_3$(001) with an adsorption energy of 2.83 eV, while VO_2(B) has stability on $SrTiO_3$(111) and sapphire(*c*-cut) with corresponding adsorption energy values of 0.91 and 1.11 eV, respectively. The optical absorption properties of the most stable (VO_2(M)@$SrTiO_3$(001) and VO_2(B)@$SrTiO_3$(111)) and less stable (VO_2(M)@sapphire(*c*-cut) and VO_2(B)@sapphire (*c*-cut)) interfaces have been assessed. Both interfaces of VO_2(M)@$SrTiO_3$(001) and VO_2(B)@$SrTiO_3$(111) showed the adsorption in visible light, while VO_2(M)@sapphire(*c*-cut) and VO_2(B)@sapphire(*c*-cut) indicated the main first adsorption peak in the infrared region of the electromagnetic light. Differences in the stability and optical behaviours of VO_2(M) and VO_2(B) interfaces on different substrates suggest a path for the creation of new symmetry-mismatched heterostructures applicable in VO_2-based electronics and optoelectronic devices.

Author contributions

Conceptualization: E. M., E. L. and P. S.; methodology: E. M. and E. L.; validation: E. M., E. L., P. S., L. P., and D. M.; investigation: E. M.; data curation: E. M.; writing – original draft preparation: E. M.; writing – review and editing: E. M., E. L., E. P., P. S., L. P., and D. M.; visualization: E. M.; supervision: P. S.; project administration: E. M., E. L., E. P., P. S., L. P. and D. M. All authors have read and agreed to the published version of the manuscript.

Conflicts of interest

There are no conflicts to declare.

Acknowledgements

This work is part of the research of H2020 (FETPROACT-EIC-05-2019) "Nanomaterials enabling smart energy harvesting for next-generation Internet-of-Things" (NANO-EH) (grant agreement no. 951761).

References

1 H. Y. Hwang, Y. Iwasa, M. Kawasaki, B. Keimer, N. Nagaosa and Y. Tokura, *Nat. Mater.*, 2012, **11**, 103–113.
2 S. U. M. Khan, M. Al-Shahry and W. B. Ingler Jr, *Science*, 2002, **297**, 2243–2245.
3 J. Jeong, N. Aetukuri, T. Graf, T. D. Schladt, M. G. Samant and S. S. P. Parkin, *Science*, 2013, **339**, 1402–1405.
4 S. Lee, T. L. Meyer, S. Park, T. Egami and H. N. Lee, *Appl. Phys. Lett.*, 2014, **105**(22), 223515.
5 C. Leroux, G. Nihoul and G. Van Tendeloo, *Phys. Rev. B*, 1998, **57**, 5111.
6 C. Wu, X. Zhang, J. Dai, J. Yang, Z. Wu, S. Wei and Y. Xie, *J. Mater. Chem.*, 2011, **21**, 4509–4517.
7 R. Basu, M. Sardar and S. Dhara, *AIP Conf. Proc.*, 2018, **1942**(1), 030003.

 © 2024 The Author(s). Published by the Royal Society of Chemistry

Open Access Article. Published on 11 March 2024. Downloaded on 7/23/2025 9:33:46 PM.
This article is licensed under a Creative Commons Attribution-NonCommercial 3.0 Unported Licence.

8 Y. Oka, S. Sato, T. Yao and N. Yamamoto, *J. Solid State Chem.*, 1998, **141**, 594–598.
9 N. Ganganagappa and A. Siddaramanna, *Mater. Charact.*, 2012, **68**, 58–62.
10 C. Wu, F. Feng, J. Feng, J. Dai, J. Yang and Y. Xie, *J. Phys. Chem. C*, 2011, **115**, 791–799.
11 Y. Wang, Z. Zhang, Y. Zhu, Z. Li, R. Vajtai, L. Ci and P. M. Ajayan, *ACS Nano*, 2008, **2**, 1492–1496.
12 B.-J. Kim, Y. W. Lee, B.-G. Chae, S. J. Yun, S.-Y. Oh, H.-T. Kim and Y.-S. Lim, *Appl. Phys. Lett.*, 2007, **90**(2), 023515.
13 L. Huitema, A. Crunteanu, H. Wong and E. Arnaud, *Appl. Phys. Lett.*, 2017, **110**(20), 203501.
14 Y. Cui, Y. Ke, C. Liu, Z. Chen, N. Wang, L. Zhang, Y. Zhou, S. Wang, Y. Gao and Y. Long, *Joule*, 2018, **2**, 1707–1746.
15 N. Ganganagappa and A. Siddaramanna, *Mater. Charact.*, 2012, **68**, 58–62.
16 E. Mohebbi, E. Pavoni, D. Mencarelli, P. Stipa, E. Laudadio and L. Pierantoni, *Front. Mater.*, 2023, **10**, 1145822.
17 E. Mohebbi, E. Pavoni, D. Mencarelli, P. Stipa, L. Pierantoni and E. Laudadio, *RSC Adv.*, 2022, **12**, 31255–31263.
18 E. Mohebbi, E. Pavoni, D. Mencarelli, P. Stipa, L. Pierantoni and E. Laudadio, *Nanoscale Adv.*, 2022, **4**, 3634–3646.
19 J. Heyd and G. E. Scuseria, *J. Chem. Phys.*, 2004, **121**, 1187–1192.
20 H. W. Verleur, A. S. Barker Jr and C. N. Berglund, *Phys. Rev.*, 1968, **172**, 788.
21 J. Lourembam, A. Srivastava, C. La-o-Vorakiat, L. Cheng, T. Venkatesan and E. E. M. Chia, *Sci. Rep.*, 2016, **6**, 25538.
22 A. Ruzsinszky, G. I. Csonka, O. A. Vydrov, G. E. Scuseria, L. A. Constantin, X. Zhou and K. Burke, *Phys. Rev. Lett.*, 2008, **100**, 136406.
23 A. Chen, Z. Bi, W. Zhang, J. Jian, Q. Jia and H. Wang, *Appl. Phys. Lett.*, 2014, **104**(7), 071909.
24 A. Srivastava, H. Rotella, S. Saha, B. Pal, G. Kalon, S. Mathew, M. Motapothula, M. Dykas, P. Yang and E. Okunishi, *APL Mater.*, 2015, **3**(2), 026101.
25 J. Jian, A. Chen, Y. Chen, X. Zhang and H. Wang, *Appl. Phys. Lett.*, 2017, **111**(15), 153102.
26 F. Shayeganfar and A. Rochefort, *Langmuir*, 2014, **30**(32), 9707–9716.
27 S. Woo, H. Jeong, S. A. Lee, H. Seo, M. Lacotte, A. David, H. Y. Kim, W. Prellier, Y. Kim and W. S. Choi, *Sci. Rep.*, 2015, **5**, 8822.
28 T. Stirner, J. Sun and M. Aust, *Phys. Procedia*, 2012, **32**, 635–639.
29 K. Krishnaswamy, C. E. Dreyer, A. Janotti and C. G. Van de Walle, *Phys. Rev. B*, 2014, **90**, 235436.
30 R. Jayan and M. M. Islam, *ACS Appl. Mater. Interfaces*, 2021, **13**, 35848–35855.
31 E. Mohebbi, E. Pavoni, L. Pierantoni, P. Stipa, G. M. Zampa, E. Laudadio and D. Mencarelli, *Results Phys.*, 2024, 107415.
32 A. Maniyar and S. Choudhary, *RSC Adv.*, 2020, **10**, 31730–31739.
33 L. Liu, N. He, T. Wu, P. Hu and G. Tong, *Chem. Eng. J.*, 2019, **355**, 103–108.
34 J. Hou, B. Wang, Z. Ding, R. Dai, Z. Wang, Z. Zhang and J. Zhang, *Appl. Phys. Lett.*, 2017, **111**, 072107.
35 B. Guo, D. Wan, A. Ishaq, H. Luo and Y. Gao, *J. Alloys Compd.*, 2017, **715**, 129–136.
36 S. Saha, T. P. Sinha and A. Mookerjee, *J. Phys.: Condens. Matter*, 2000, **12**, 3325.
37 A. K. Harman, S. Ninomiya and S. Adachi, *J. Appl. Phys.*, 1994, **76**, 8032–8036.
38 M. Schubert, T. E. Tiwald and C. M. Herzinger, *Phys. Rev. B*, 2000, **61**, 8187.
39 S. Smidstrup, T. Markussen, P. Vancraeyveld, J. Wellendorff, J. Schneider, T. Gunst, B. Verstichel, D. Stradi, P. A. Khomyakov and U. G. Vej-Hansen, *J. Phys.: Condens. Matter*, 2019, **32**, 015901.
40 H. S. Yu, S. L. Li and D. G. Truhlar, *J. Chem. Phys.*, 2016, **145**(13), 130901.
41 F. Favot, A. Dal Corso and A. Baldereschi, *J. Chem. Phys.*, 2001, **114**, 483–488.
42 M. J. van Setten, M. Giantomassi, E. Bousquet, M. J. Verstraete, D. R. Hamann, X. Gonze and G.-M. Rignanese, *Comput. Phys. Commun.*, 2018, **226**, 39–54.
43 E. Laudadio, E. Mohebbi, E. Pavoni, C. Minnelli, S. Sabbatini and P. Stipa, *Colloids Surf., A*, 2023, **667**, 131388.
44 E. Pavoni, E. Mohebbi, P. Stipa, L. Pierantoni, D. Mencarelli, M. Dragoman, M. Aldrigo and E. Laudadio, *Nanoscale Adv.*, 2023, **5**, 2748–2755.
45 L. Goerigk, *Non-Covalent Interact. Quantum Chem. Phys.*, 2017, 195–219.
46 F. Sedona, M. M. S. Fakhrabadi, S. Carlotto, E. Mohebbi, F. De Boni, S. Casalini, M. Casarin and M. Sambi, *Phys. Chem. Chem. Phys.*, 2020, **22**, 12180–12186.
47 G. P. Chen, V. K. Voora, M. M. Agee, S. G. Balasubramani and F. Furche, *Annu. Rev. Phys. Chem.*, 2017, **68**, 421–445.
48 K. Kolwas and A. Derkachova, *Nanomaterials*, 2020, **10**, 1411.
49 T. Micklitz, A. Morningstar, A. Altland and D. A. Huse, *Phys. Rev. Lett.*, 2022, **129**, 140402.
50 E. Mohebbi and M. M. S. Fakhrabadi, *J. Mater. Sci. Eng. B*, 2022, **281**, 115745.